Energy 182 (2019) 802–813

Contents lists available at ScienceDirect

Energy

journal homepage: www.elsevier.com/locate/energy

Clean and stable utilization of solar energy by integrating dish solar Stirling engine and salinity gradient technology

Xiaotian Lai, Minjie Yu, Rui Long*, Zhichun Liu, Wei Liu**

School of Energy and Power Engineering, Huazhong University of Science and Technology, 1037 Luoyu Road, Wuhan, 430074, China

ARTICLE INFO

Article history:
Received 8 January 2019
Received in revised form
23 May 2019
Accepted 11 June 2019
Available online 12 June 2019

Keywords:
Dish solar Stirling engine
Salinity gradient
Energy storage
Clean energy utilization

ABSTRACT

A hybrid energy utilization system, integrating dish solar SE and salinity gradient based energy storage system, was proposed to realize clean and stable power generation from solar energy. Power output of dish solar Stirling engine was utilized to pressurize the salt water into RO (reverse osmosis) for storing the energy in the form of concentration gradient, and stable power output was generated from the concentration gradient via PRO (pressure retarded osmosis). The system performance was systematically investigated under the ideal and non-ideal models, to evaluate the theoretical and realistic energy conversion ability. Results indicate that higher initial concentration presents better energy efficiency, for it has slower decreasing slope of transmembrane water flux in PRO. Optimal RO and PRO operating pressure exist for achieving the maximal energy efficiency. The ideal maximal overall energy conversion efficiency reaches 9.23% within the research scope. With the detrimental factors being considered, the maximal overall efficiency of 5.07% is achieved.

© 2019 Elsevier Ltd. All rights reserved.

1. Introduction

The rapid consumption of fossil fuels and accompanying pollution problems such as the emission of greenhouse gas, NO_x and SO_x influence human society significantly [1]. Numerous researches such as clean combustion [2], low temperature heat utilization [3], sustainable energy exploitation [4], novel hybrid energy system [5,6] and heat transfer enhancement [7,8] in recent decades were conducted as powerful response. Solar energy, the original energy source which is of tremendous amount and totally clean, is regarded as one of prospective methods to mitigate these problems [9]. It is mainly categorized into two types of photovoltaic and solar thermal utilization [10]. Photovoltaic technology has the advantage of better system simplicity while solar thermal technology generally achieves higher solar-electric conversion efficiency. As to solar thermal utilization, common configurations of trough, tower and dish are widely utilized to focus sunshine to obtain high temperature for driving thermodynamic cycles. Compared with the other two, dish configuration requires less space and has higher concentration ratio to produce thermal energy with high temperature level. Hence, it is utilized to drive some small-scale thermodynamic cycles such as Brayton [11] and Stirling cycles [12]. For SE has higher theoretical thermal efficiency and operates with less noise [13,14], dish solar SE has been attracting considerable attention since its invention in 1987 by Roelf J. Meijer.

Mohammad Hossein Ahmadi et al. analyzed the theoretical performance of dish solar SE and optimized the operating temperatures to achieve the compromise of power output and thermal efficiency with three different decision methods in Ref. [15]. Results indicate optimal temperatures decided by LINMAP approaches the ideal solution most closely. Furthermore, entransy loss and entropy generation rate were considered as additional optimization targets to achieve more comprehensive optimal performance in Ref. [16]. Fatih Aksoy et al. conducted an experiment of a beta type SE which operates with halogen lamp as solar simulator. The performance was tested under the lamp power of 400 and 1000 W respectively. Higher lamp power achieves better engine power of 127.17 W, torque of 3.4 Nm and efficiency of 12.85% [17]. G.E. Carrillo Caballero et al. modeled and investigated the performance of a dish solar SE with directly illumined receiver. Their research indicates radiative loss in receiver is significant which occupies 96.06% in the total heat loss under low wind speed condition. Furthermore, optimal efficiency of 21% and power output of 11.1 kW were obtained with multi-objective algorithm [18]. Ana C. Ferreira et al. evaluated and optimized the thermal and economic performance of a dish solar SE

* Corresponding author.
** Corresponding author.
E-mail addresses: r_long@hust.edu.cn (R. Long), w_liu@hust.edu.cn (W. Liu).

https://doi.org/10.1016/j.energy.2019.06.082
0360-5442/© 2019 Elsevier Ltd. All rights reserved.

based micro cogeneration system. Optimization algorithm of GPS (generalized pattern search) was employed in order to maximize the system annual worth. Results indicate that electrical and thermal power of 3.65 kW and 11.06 kW can be obtained with an attractive economic performance [19]. It can be seen dish solar SE is feasible to convert the solar energy into electricity with remarkable ability. However, one of the main barriers is the intermittency of incident solar energy with time and limits the further development of dish solar SE. Energy storage system is one of the efficient methods to solve this problem. Y. Kadri et al. investigated the performance of dish solar SE coupled with lead acid battery. Battery was utilized to meet the insufficient power of SE when sunshine intensity drops with daily time. Results indicate this hybrid system is capable to meet the custom demand continuously and achieve efficient energy balance of subsystems with the maintain of link voltage [20]. Compared with CAES (compressed air energy storage) and PHS (pumped hydro storage), battery is independent on the geometrical condition and has more flexible compacity, but the toxicity and potential pollution risk still require further improvement.

In the recent years, a salinity gradient based energy storage system was proposed and attracted some attention for the substance is easily obtainable and has extremely slight effect on environment [21,22]. The sustainable energy is utilized to generate concentration difference via RO, then released by PRO to generate stable power output. As a membrane filtration technology, RO is widely utilized for fresh water production [23] and waste water treatment [24]. It is noteworthy that not only fresh water can be generated in RO, but considerable Gibbs free energy is also stored in the form of concentration difference simultaneously. This energy is capable to be released by PRO to generate shaft power [25,26], and the first PRO plant was constructed in 2009 as well [27]. The fundamental thermodynamic analysis conducted by Ngai Yin Yip et al. clarified the relationship of frictional loss, extractable power and outlet residual concentration difference in PRO precisely, and indicated that PRO has competitive efficiency of 60% with river and sea solutions [28]. Jeri L. Prante utilized PRO to harvest the Gibbs free energy from RO module and reduce the energy consumption for salt water desalination. With the integration of PRO, the SEC (specific energy consumption) drops significantly by 40% from 2.0 to 1.2 $kW \cdot h/m^3$ under a recovery rate of 50% [29]. Chun Feng Wan et al. proposed a closed loop SWRO (sea water reverse osmosis) by employing PRO to reduce the specific energy consumption. Compared with the configuration of single RO module, the further installment of PX (pressure exchanger) and PRO module reduces the SEC from 5.51 to 1.79 and 1.08 $kW \cdot h/m^3$ respectively [30]. The significant energy consumption drop indicates the outlet concentration difference of RO has great potential to be released by PRO. Hence, Wei He et al. [21] and Rui Long et al. [22] both evaluated the energy conversion ability of RO and PRO based energy storage system, the results indicate that it is feasible and has acceptable efficiency.

Hence, in order to solve the intermittency of solar energy with a cleaner method. A hybrid system which utilizes a closed loop salinity gradient based energy storage system to stabilize the power output of dish solar SE was proposed. For dish solar Stirling engine operates with low capacity but requires less space consumption, it is suitable to be utilized for remote small-scale off-grid power generation. In addition, the substance of NaCl solution for energy storage and release is extremely easily acquirable and eco-friendly. Hence, this hybrid system can be a potential clean and stable power generation method from sunshine for small scale distributed household. With the establishment of the corresponding mathematical models and algorithm under ideal and non-ideal conditions, the energy conversion ability was investigated systematically to evaluate the ideal energy conversion limitation and the realistic ability with current technology ability. The influence mechanism of initial concentration, operating pressures of RO and PRO on energy conversion efficiency was analyzed and optimized to achieve the maximum within the scope of this study. The influence of detrimental factors such as the imperfect regeneration, friction loss and concentration polarization on the system performance was investigated as well. Finally, some meaningful conclusions were drawn.

2. System description and mathematical model

2.1. System description

As depicted in Fig. 1, this hybrid system consists of three main subsystems those are dish solar SE module, energy storage module and energy release module respectively. In dish solar SE, as the concentrated sunlight from concentrator focuses on receiver, solar energy converts into thermal energy with high temperature. Then driven by the temperature difference, thermal energy transfers into the heater of SE, to heat the charged gas and motivate SE to generate shaft power for driving the pump.

The energy storage module is composed of pressure exchanger, RO device and three tanks. The effluent brine water from Tan_M with an initial concentration of C_{in}, separates into two streams for concentrating and diluting in RO respectively. Stream S_{14} (to be diluted) flows into RO directly while stream S_2 (to be concentrated) needs to be pressurized in advance. PX is installed to harvest the residual pressure in effluent concentrated flow from RO, for pre-pressurizing stream S_2. Then, pump provides the net energy requirement for pressure elevation in RO. Driven by the hydraulic pressure difference aside the semipermeable membrane, transmembrane water flux occurs and leads to the appearance of concentration difference between two streams. Hence, in energy storage module, the shaft power from SE is converted into the high pressure of concentrated solution and Gibbs free energy sequentially, then stored in tank Tan_L and Tan_H.

In energy release module, the solution with high concentration gets pressurized by PX and feeds into PRO. Driven by the osmotic pressure difference between two solutions, water transfers from the solution of low concentration to the high side. The extracted water flows into a hydro turbine to generate stable electricity output, and the residual stream goes through PX for pressurizing stream S_7. Finally, three streams S_{11}, S_{13} and S_{17} flow into the tank Tan_M simultaneously, the concentration of brine water returns to the initial value. Thus, a salinity gradient based closed loop cycle can be established to stabilize the power output of dish solar SE system.

2.2. Mathematical model and algorithm

The ideal model of dish solar SE is established based on the adiabatic model of SE stated in Appendix. A1 and the energy balance equations at hot and cold ends as follows.

$$\dot{Q}_{H,Supplement} = \dot{Q}_{H,Transfer} = \dot{Q}_{H,Load} \tag{1}$$

$$\dot{Q}_{L,Supplement} = \dot{Q}_{L,Transfer} = \dot{Q}_{L,Load} \tag{2}$$

In heater, the heat supplement is the utilizable thermal energy from receiver in Eq. (3). The heat transferred is the production of heat transfer ability (K_H) and temperature difference between receiver and substance in the form of Eq. (4). In addition, the heat load in heater is the thermal requirement for heating substance which is a function of T_h and T_l in Eq. (5) according to the adiabatic

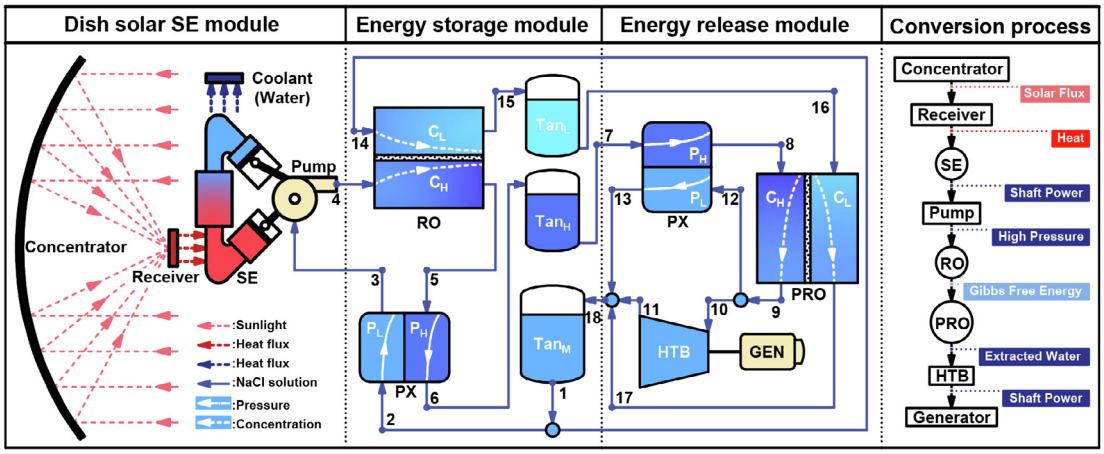

Fig. 1. Schematic view of the hybrid system.

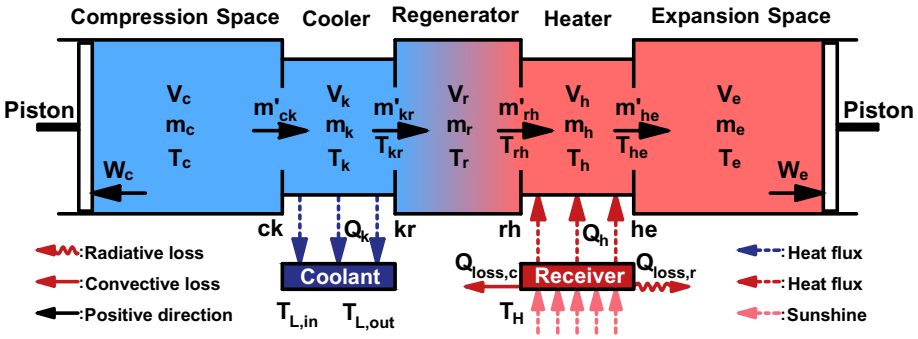

Fig. 2. Control volumes of dish solar SE.

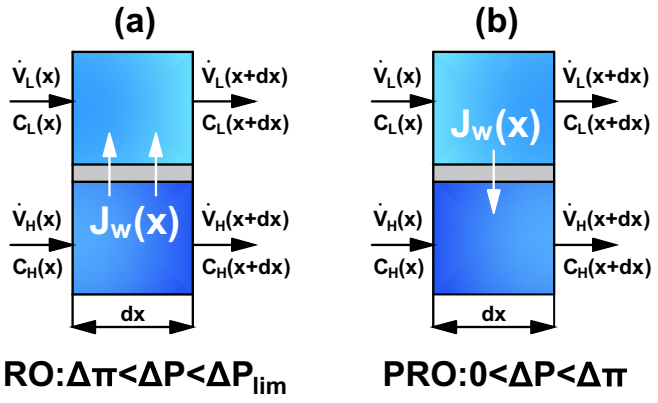

Fig. 3. Transmembrane water flux in RO and PRO.

analysis.

$$\dot{Q}_{H,Supplement} = IA_R C\eta_{optical} - h_c A_R (T_H - T_0) - \varepsilon\sigma A_R \left(T_H^4 - T_{sky}^4\right) \tag{3}$$

$$\dot{Q}_{H,Transfer} = K_H (T_H - T_h) \tag{4}$$

$$\dot{Q}_{H,Load} = \dot{Q}_h = f(T_h, T_l) \tag{5}$$

As to the cooler, the heat supplement is the heat released from SE which is obtained from the adiabatic analysis as well. Considering the coolant has a finite heat capacity, the heat transfer in cooler is expressed as the production of heat transfer ability (K_L) and logarithmic mean temperature difference in Eq. (7). The heat undertaken by the coolant is expressed as the enthalpy increase of coolant in Eq. (8).

$$\dot{Q}_{L,Supplement} = \dot{Q}_k = f(T_h, T_l) \tag{6}$$

$$\dot{Q}_{L,Transfer} = -K_L \frac{(T_l - T_{L,in}) - (T_l - T_{L,out})}{\ln\left(\frac{T_l - T_{L,in}}{T_l - T_{L,out}}\right)} \tag{7}$$

$$\dot{Q}_{L,Load} = -\dot{m}_w c_{p,w} (T_{L,out} - T_{L,in}) \tag{8}$$

For a dish solar SE with specific geometrical and operational parameters, Eqs. (3)–(8) indicate the heat supplement, transfer and requirement in heater and cooler can be written as the function of four undetermined temperatures of T_H, T_h, T_l and $T_{L,out}$ which depend on the system size and operating condition. Meanwhile, Eqs. (1) and (2) indicate four independent equations exist and can be utilized to solve the four undetermined temperatures with corresponding algorithm in Fig. 4, to achieve the steady operation of dish solar SE. With the power output and energy consumption in each module being quantified, the energy efficiencies in dish solar SE module can be evaluated as follows.

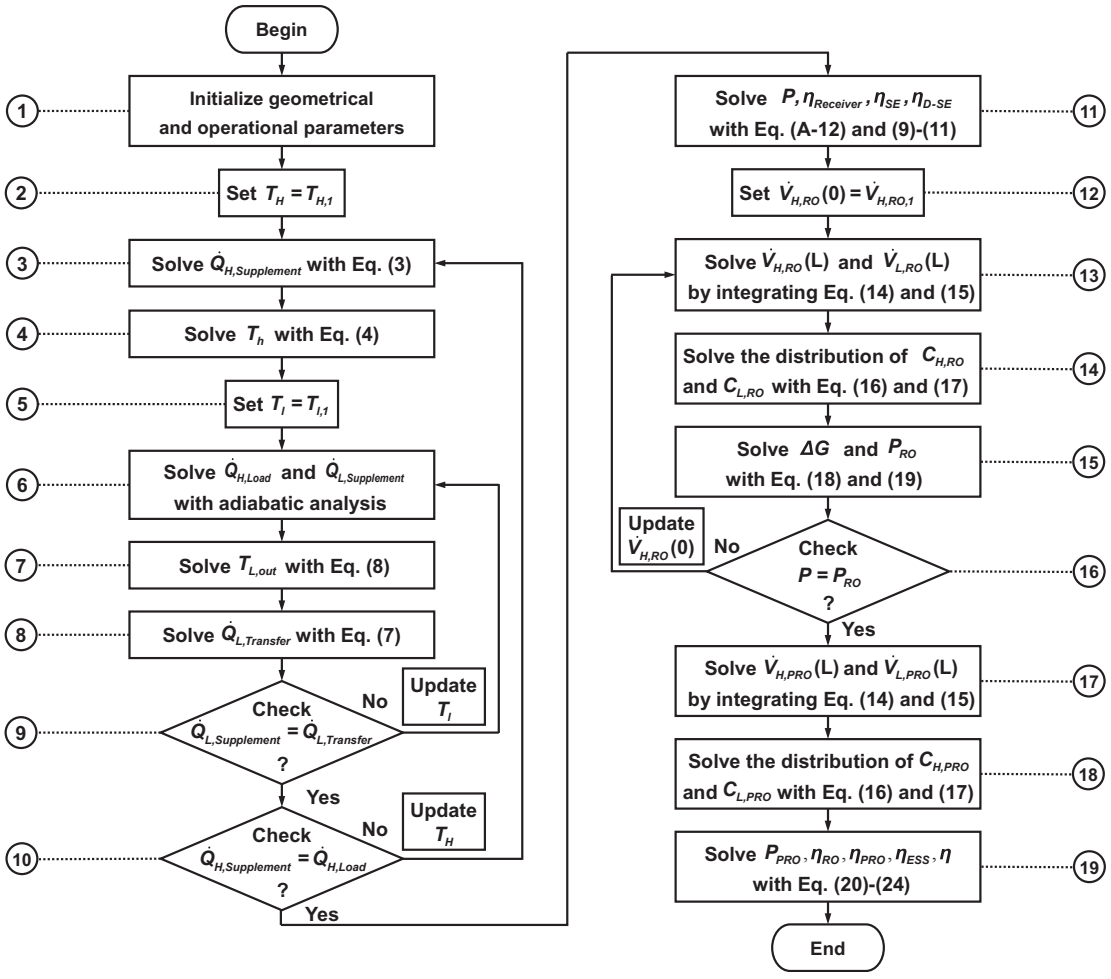

Fig. 4. Algorithm flow chart.

$$\eta_{Receiver} = \frac{\dot{Q}_{H,Load}}{IA_R C \eta_{optical}} \tag{9}$$

$$\eta_{SE} = \frac{P}{\dot{Q}_{H,Load}} \tag{10}$$

$$\eta_{DS-SE} = \frac{P}{IA_R C} = \eta_{optical}\eta_{Receiver}\eta_{SE} \tag{11}$$

In the energy storage and release system, the governing equations of RO and PRO are familiar but with different net driving force. The ideal membranes required in RO and PRO are both semi-permeable membranes which only allow the permeation of water flux. Water flux permeates from the highly pressurized concentrated side to the diluted side in RO, and permeates from the diluted side into the slightly pressurized concentrated side in PRO driven by the net osmotic pressure difference. The infinitesimal control volumes are depicted in Fig. 3 and the equations of transmembrane water flux are stated in Eqs. (12) and (13).

$$J_{w,RO}(x) = A_{RO}(\Delta P_{RO}(x) - \Delta\pi_{RO}(x)) \tag{12}$$

$$J_{w,PRO}(x) = A_{PRO}(\Delta\pi_{PRO}(x) - \Delta P_{PRO}(x)) \tag{13}$$

As water flux pierces through the membrane, the distribution of volume flow rate and concentration along the flow direction can be calculated according to Eq. (14)–(17) (RO: $i = -1$, PRO: $i = 1$) with the initial values specified previously.

$$\frac{d\dot{V}_H(x)}{dx} = iWJ_w(x) \tag{14}$$

$$\frac{d\dot{V}_L(x)}{dx} = -iWJ_w(x) \tag{15}$$

$$C_H(x) = C_H(0)\frac{\dot{V}_H(0)}{\dot{V}_H(x)} \tag{16}$$

$$C_L(x) = C_L(0)\frac{\dot{V}_L(0)}{\dot{V}_L(x)} \tag{17}$$

With the variation of solution concentration, the energy stored in the form of Gibbs free energy can be expressed as Eq. (18) [31]. $C_{M,RO}(L)$ is the concentration of the mixture of two effluent streams from RO.

$$\Delta G = 2RT\left[\dot{V}_{H,RO}(L)C_{H,RO}(L)\ln\frac{C_{H,RO}(L)}{C_{M,RO}(L)} + \dot{V}_{L,RO}(L)C_{L,RO}(L)\ln\frac{C_{L,RO}(L)}{C_{M,RO}(L)}\right] \tag{18}$$

The net energy consumption in RO is the difference of energy required for pressure elevation and energy harvested from the effluent flow by pressure exchanger. The power output of PRO depends on the extracted water flow rate and operating pressure.

$$P_{RO} = \Delta P_{RO}\dot{V}_{H,RO}(0) - \eta_{ERD}\Delta P_{RO}\dot{V}_{H,RO}(L) \tag{19}$$

$$P_{PRO} = \Delta P_{PRO}\left[\dot{V}_{H,PRO}(0) - \dot{V}_{H,PRO}(L)\right] \tag{20}$$

As the energy input and output of each subsystem is determined, the local and overall efficiencies can be evaluated according to Eq. (21)–(24) as well.

$$\eta_{RO} = \frac{\Delta G}{P_{RO}} \tag{21}$$

$$\eta_{PRO} = \frac{P_{PRO}}{\Delta G} \tag{22}$$

$$\eta_{ESS} = \frac{P_{PRO}}{P_{RO}} \tag{23}$$

$$\eta = \frac{P_{PRO}}{IA_HC} \tag{24}$$

The corresponding algorithm is depicted in Fig. 4 for stating a more precise insight view of calculation procedures. As step 1 initialized the geometrical and operational parameters, steps 2–11 are set to achieve the steady operation of dish solar SE by iterating T_H and T_l. The convergence of T_l in steps 6–9 represents the energy balance between charged gas and cooling water is achieved. Similarly, the convergence of T_H in steps 3–10 represents the energy balance between solar receiver and SE is achieved. Thus, the power output and energy efficiencies of dish solar SE can be evaluated at step 11. Successively, an appropriate inlet volume flow rate is determined with steps 12–16 to match the net energy consumption of RO and energy supplied by dish solar SE. The corresponding outlet values of concentration and flow rate in RO can be obtained then specified as the initial values of PRO module. Governed by the differential equations Eq. (14)-(17), the stable power output of PRO and energy conversion efficiencies can be obtained after the calculation of extracted water flowrate with steps 17–19.

3. Results and analysis

3.1. Evaluation of theoretical performance

Theoretical model illustrates the fundamental principle that energy conversion procedure follows. Some improvable detrimental factors such as optical loss, regenerative heat loss, power loss originated from the flow friction in engine and concentration polarization phenomenon in RO and PRO are neglected to evaluate the ideal system performance with the initial values set in Table 1.

In dish solar SE, T_H increases to drive the thermal energy into heat engine as the concentrated solar flux illuminates on solar receiver. Meanwhile, convective and radiative heat losses exist due to the temperature difference between receiver and environment. T_H of 1590 K is achieved as the dish solar SE operates steadily with a solar power input of 47.93 kW. The blue bars above the dash line in Fig. 5-(a) illustrates the energy distribution at receiver. It can be seen the convective and radiative losses occupy 1.49% and 38.60% respectively. The radiative loss is more significant for it is positively related to the fourth powder of T_H. The residual 59.91% of input solar energy is converted into utilizable heat and transferred to motivate the heat engine for generating shaft power.

In heat engine, substance temperature is elevated to 1447 K heated by the receiver. Then hot gas expands sufficiently to achieve a cyclic expansion work of 1147.53 J encircled by the red dot curve in Fig. 5-(b). And the area encircled by the blue dot curve indicates that the compressed cold gas consumes 319.66 J in a thermodynamic cycle. Finally, net power output of 20.70 kW is generated and occupies 43.18% of the entire incident solar energy while the emitted heat in cooler occupies 16.73%.

Sequentially, the shaft power is stored as Gibbs free energy in RO and released as stable shaft power in PRO. From Table 2, as the transmembrane water flux permeates through the membrane in RO, salt solution with initial concentration of 0.5 M is concentrated to 0.84 M and diluted to 0.36 M respectively. Gibbs free energy of 9.05 kW is stored with the efficiency of 43.71% equivalently. As the concentrated and diluted solutions flow through PRO module, the concentration difference drops to release a stable power output of 4.06 kW with the efficiency of 44.83%. It is noteworthy that the integration of energy storage system is capable to stabilize the energy output of dish solar SE, but the increase of system complexity also reduces the overall energy conversion efficiency. Thus, achieving the maximal efficiency of ESS is essential for evaluating the optimal overall performance.

Energy storage and release in RO and PRO module rely on the variation of solution concentration which is driven by the transmembrane water flux. For the net driving force associates closely with the osmotic and hydraulic pressure difference, the initial concentration of NaCl solution and operating pressure influence

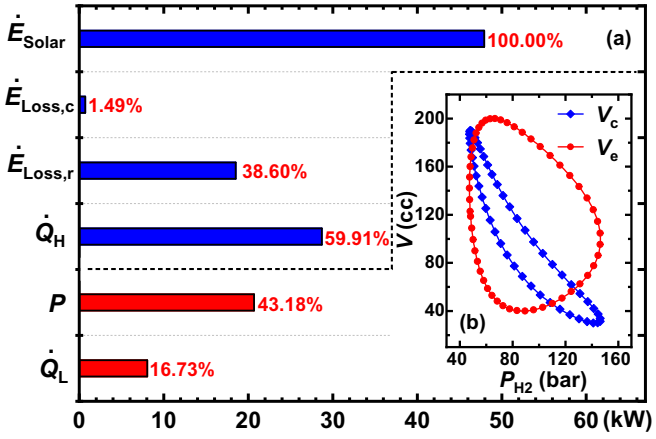

Fig. 5. Energy distribution in dish solar SE of sample calculation.

Table 1
Initial values set for sample calculation.

Dish solar SE system							
$A_{Dish}(m^2)$	$A_R(m^2)$	Gas (−)	F (Hz)	$I(W/m^2)$	$V_{wind}(m/s)$	$\eta_{optical}(\%)$	$\varepsilon(\%)$
53	0.058	H_2	25	906	1	100	100
Energy storage and release system							
$L_{RO}(m)$	$W_{RO}(m)$	$A_{RO}m/(s\cdot Pa)$	$N_{RO}(-)$	$L_{PRO}(m)$	$W_{PRO}(m)$	$A_{PRO}m/(s\cdot Pa)$	$N_{PRO}(-)$
2	1	1.19e-11	400	5	3	1.87e-12	400

Table 2
Energy storage and release performance of sample calculation.

$C_{RO,H,out}(M)$	$C_{RO,L,out}(M)$	$\Delta G_{RO,out}$(kW)	η_{RO}(%)
0.84	0.36	9.05	43.71
$C_{PRO,H,out}(M)$	$C_{PRO,L,out}(M)$	$P_{PRO,out}$(kW)	η_{PRO}(%)
0.67	0.40	4.06	44.83

the performance of ESS. η_{ESS} in Eq. (23) evaluates the fraction of stabilized energy output in the mechanical energy input and η in (24) represents the overall energy conversion efficiency. Fig. 6 depicts the η_{ESS} and η under different operating pressure and initial solution concentration. It can be seen that higher initial concentration contributes to better energy efficiency, η_{ESS} and η gets improved by around 2.5% and 1.0% as initial concentration increases from 0.4 M to 0.6 M.

Compare the transmembrane water flux distribution in PRO with different initial concentration under specified ΔP_{RO} and ΔP_{PRO} in Fig. 7. It can be seen that for the membrane area is sufficient, specified ΔP_{RO} achieves the same initial osmotic pressure difference in PRO which equals to ΔP_{RO}. However, higher C_{in} corresponds to higher initial draw solution concentration in PRO which is depicted in Fig. 7-(b). Beginning with the same transmembrane water flux, higher initial draw solution concentration in PRO is more difficult to be interrupted. Hence, the transmembrane water flux drops more slowly along the flow direction under a higher C_{in} which is consistent with Fig. 7-(a). Meanwhile, the production of the area in grey beneath the transmembrane water flux curve and membrane width represents the flow rate of extracted water in a single PRO unit. It can be seen C_{in} of 0.6 M occupies larger area and then induces more total extracted water and power output in Fig. 7-(c).

Furthermore, with the increase of RO and PRO operating pressure, η_{ESS} and η vary in the range of 12–21% and 5–9% with a trend of decreasing after increasing in Fig. 6. From Fig. 8-(a), it can be seen that the increase of RO operating pressure can improve the outlet concentration difference of RO, then provides stronger initial driving force for transmembrane water flux in PRO. As ΔP_{RO} increases from 2.5 MPa to 2.9 MPa, the corresponding red and black water flux curves indicate ΔP_{RO} of 2.9 MPa achieves more fresh water extraction (red area difference of R+ and R-) with the improvement of initial driving force. When ΔP_{RO} further increases to 4.0 MPa, the pumped feed solution into RO drops significantly as well, for the power input from SE is constant. Thus, the initial flow rate of draw solution in PRO drops sequentially as depicted in Fig. 8-(b). Comparing the black and blue water flux curves in Fig. 8-(a), it tells that stronger ΔP_{RO} of 4.0 MPa leads the transmembrane water flux in PRO to drop sharply and vanish quickly. The reason is that lower initial flow rate is easier to be interrupted by stronger initial driving force. Hence, water flux under ΔP_{RO} of 2.9 MPa exceeds that under ΔP_{RO} of 4.0 MPa after the blue dot, then achieves more extracted water (blue area difference of B+ and B-) and power output in Fig. 8-(c). Namely, the optimal RO operating pressure represents a state point at which the initial osmotic pressure difference and flow rate of draw solution in PRO are both relatively high to result in strong initial driving force and low decreasing speed of draw solution concentration simultaneously. On the other hand, optimal PRO operating pressure represents the most appropriate point of transmembrane water flow rate and hydraulic pressure difference. For high ΔP_{PRO} increases the specific power output ability of PRO but reduces the net extracted water, and low ΔP_{PRO} increases the amount of extracted water but reduces the specific power output ability of PRO.

In order to evaluate the optimal system performance under maximal efficiency, numerical optimization algorithms of GA (genetic algorithm) and PSO (particle swarm optimization) were employed to optimize the operating pressure, for the nonlinearity

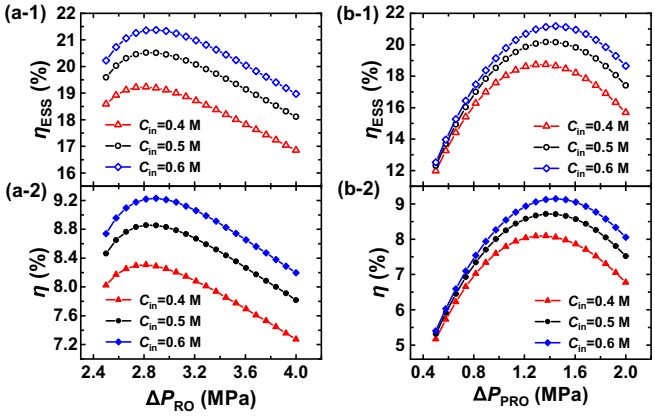

Fig. 6. Efficiency as a function of operating pressure in RO and PRO under different initial concentration of NaCl aqueous solution.

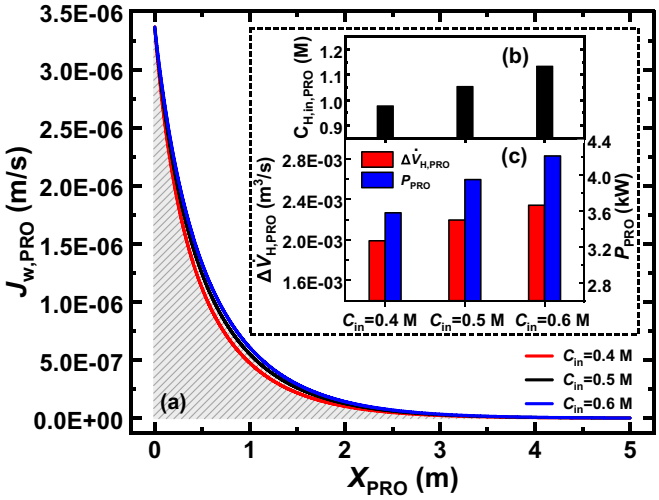

Fig. 7. Performance comparison under different initial concentration of NaCl solution.

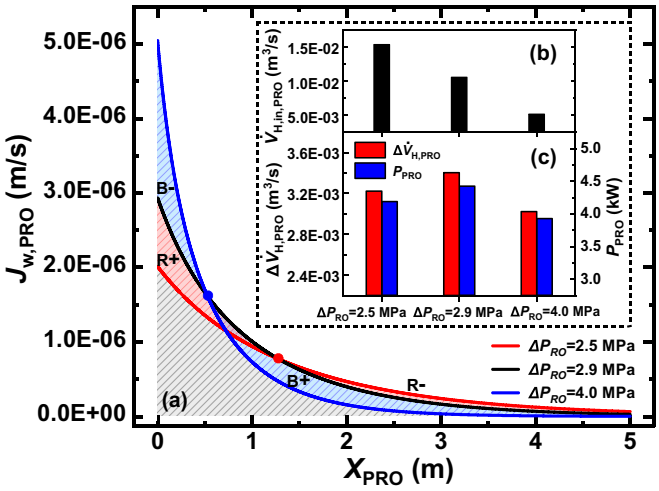

Fig. 8. Performance comparison under different operating pressure in RO.

In order to evaluate the optimal system performance under maximal efficiency, numerical optimization algorithms of GA (genetic algorithm) and PSO (particle swarm optimization) were employed to optimize the operating pressure, for the nonlinearity

Table 3
System optimal efficiency under ideal condition.

C_{in}(M)	Algorithm (−)	ΔP_{RO}(MPa)	ΔP_{PRO}(MPa)	$\eta_{ESS,max}$(%)	η(%)	Time (−)
0.4	GA	2.60	1.07	19.27	8.32	8 h 47min
	PSO	2.68	1.17	19.36	8.36	4 h 36min
0.5	GA	2.76	1.25	20.53	8.86	10 h 30min
	PSO	2.80	1.25	20.54	8.87	4 h 26min
0.6	GA	2.92	1.32	21.38	9.23	8 h 57min
	PSO	2.89	1.32	21.38	9.23	4 h 47min

of the mathematical model. Results are listed in Table 3, it can be seen the optimal results achieved by GA and PSO are generally consistent while PSO requires only around half of the time consumption of GA. Maximal energy conversion efficiencies under the initial concentration of 0.4, 0.5 and 0.6 M are 19.36%, 20.54% and 21.38% respectively. The corresponding overall efficiencies are 8.36%, 8.87% and 9.23%. Equivalently, maximal stabilized power output of 4.42 kW can be generated as ESS operates under the maximal efficiency condition with the initial concentration of 0.6 M.

Plotting the corresponding concentration distribution diagram in Fig. 9, the concentration of concentrated and diluted solutions varies from 0.60 M to 1.01 and 0.43 M respectively in energy storage process. Meanwhile, Gibbs free energy of 9.35 kW is stored. Then as the concentrated and diluted solutions flow into energy release module, extracted water drives the hydro turbine to generate stable power output. Meanwhile, the concentration of two streams vary to 0.76 and 0.49 M. It can be seen the residual unextractable Gibbs free energy in PRO originated from the applied hydraulic pressure difference is considerable which leads to the relatively low energy efficiency. For rationally releasing Gibbs free energy and improving the energy efficiency, multi-stage PRO configuration or additional RED (reverse electrodialysis) device can be installed and further investigated.

3.2. Evaluation of current performance

In this part, the aforementioned detrimental factors such as the optical loss, heat regeneration and pressure loss in heat engine, concentration polarization in RO and PRO are considered to give a more realistic performance evaluation. The corresponding models were validated with relative experimental researches in Appendix as well.

In Fig. 10, the ideal and non-ideal energy distribution in dish solar SE are compared under the same geometrical and operational conditions. As to the optical module in Fig. 10-(a), the realistic performance has an optical efficiency which considers the optical loss originated from the imperfect reflection of concentrator and optical interception at the receiver entrance. With less solar flux illuminating on the receiver, receiver temperature drops to 1128 K. Hence, convective and radiative heat losses both decrease with the drop of temperature difference between receiver and environment. It can be seen the radiative loss drops significantly from 38.60% to 9.73%. Consequentially, though optical loss occupies considerable part of the incident solar energy, the drop of receiver heat loss is significant as well. Thus, more heat is supplied to the engine which occupies 67.95% of the solar energy, to meet the heat demand of isothermal heat absorbing and imperfect heat regeneration. However, lower receiver temperature also induces lower heat absorbing temperature which is 965 K under a specified heat transfer ability at hot end. Then it leads to weaker gas expansion compared with the ideal condition as illustrated by the red curves in Fig. 10-(b). Meanwhile, the blue curves indicate that the consumed compressed work varies slightly between two conditions. Under the non-ideal condition, more heat is required to be released into the environment due to the additional regeneration heat loss. The total emitted heat occupies 42.39% of the incident solar energy. Hence, heat releasing temperature is higher and induces a plumper V–P diagram though the average pressure decreases slightly. By subtracting the power consumption for gas compression and power loss by flow friction from the expansion power, net power output of heat engine drops to 12.25 kW which is 25.56% of the total solar energy. The drop of power output and efficiency in dish solar SE will influence the performance of downstream ESS and overall system sequentially.

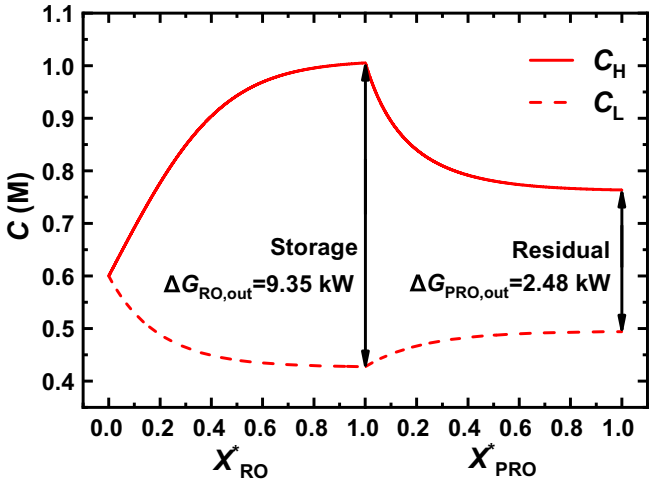

Fig. 9. Concentration distribution along the flow direction in RO and PRO modules under optimal condition.

With the concentration polarization in RO and PRO being considered, the performance of ESS was optimized targeting with the maximal efficiency as well. PSO was employed for it requires less time consumption to obtain the optimal value, and the results are stated in Table 4. Compared with the ideal condition, it can be seen the optimal ΔP_{RO} increases while the optimal ΔP_{PRO} decreases.

In RO module, as water flux pierces from the concentrated side to diluted side, concentration polarization aggravates the osmotic pressure difference. Then water flux in RO decreases with the drop of net driving force. The blue curve in Fig. 11-(a) illustrates the distribution of transmembrane water flux under the ideal condition. It can be seen the area beneath the blue curve is considerably large to achieve high outlet concentration difference in RO. However, as utilizing the same ΔP_{RO} of 2.89 MPa under the non-ideal condition (black curve), water flux drops significantly with the increase of osmotic pressure difference. This is unfavorable for achieving high outlet concentration difference. Hence, the optimal ΔP_{RO} under non-ideal condition should increase to improve the transmembrane water flux which is plotted with the red curve in Fig. 11-(a). With the aforementioned analysis, the optimal ΔP_{RO} corresponds to an appropriate operating state at which the ΔP_{RO} and flow rate of salt water are both relatively high. Meanwhile, the detrimental factors in dish solar SE reduces the power input for ESS as well which means less salt water can be pumped. Thus, the

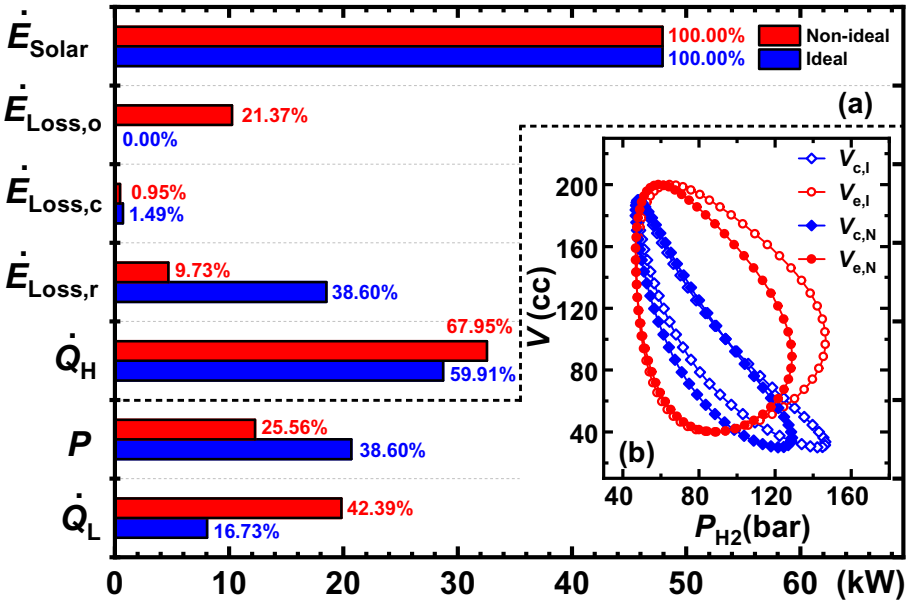

Fig. 10. Dish solar SE energy distribution comparison under ideal and non-ideal conditions.

Table 4
System optimal efficiency under non-ideal condition.

C_{in}(M)	Algorithm (−)	ΔP_{RO}(MPa)	ΔP_{PRO}(MPa)	$\eta_{ESS,max}$(%)	η(%)	Time (−)
0.4	PSO	2.89	1.04	14.40	4.68	3 h 36min
0.5	PSO	3.17	1.17	15.10	4.91	3 h 42min
0.6	PSO	3.43	1.30	15.59	5.07	4 h 31min

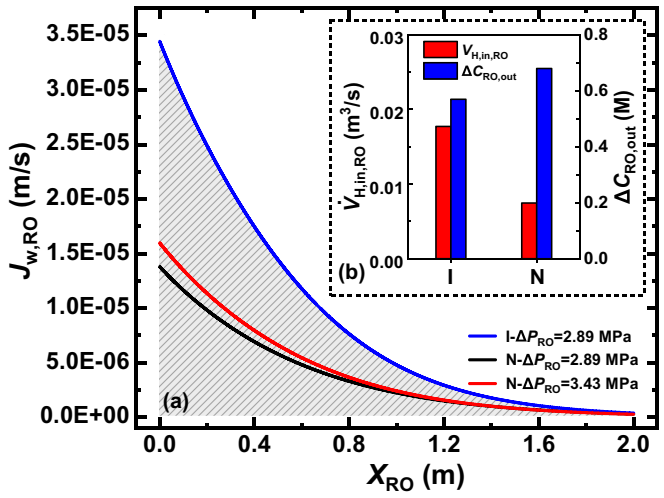

Fig. 11. Performance comparison of RO under ideal and non-ideal condition.

optimal ΔP_{RO} under the non-ideal condition only increases in some extent, to achieve an appropriate flow rate and CP reduction simultaneously. For the lower flow rate depicted with the red bar in Fig. 11-(b) is easier to be interrupted, though the transmembrane water flux under non-ideal condition is weaker, the variation of concentration difference is more obvious. Finally, the outlet concentration difference of RO under non-ideal condition is higher in Fig. 11-(b), which is beneficial for PRO. When water flux pierces from the diluted side to the concentrated side in PRO, the membrane osmotic pressure difference is reduced by the concentration polarization in PRO. Higher initial bulk concentration difference is capable to offset part of this negative effect. Hence, the optimal ΔP_{PRO} under non-ideal condition decreases slightly.

As to the efficiency of ESS, the concentration polarization increases the resistance for transmembrane water flux and limits the energy conversion ability of RO and PRO consequentially. For the solution with an initial concentration of 0.6 M, Fig. 12-(a) indicates the efficiency of RO and PRO both drop from 45.21% and 47.29% to 41.15% and 37.88% respectively as compared with the ideal condition. The corresponding concentration distribution and outlet Gibbs free energy are illustrated in Fig. 12-(b), it can be seen though the bulk outlet concentration difference in RO under non-ideal condition is larger, lower flow rate and CP both reduce the stored Gibbs free energy to 5.04 kW with a power input of 12.25 kW. Then in PRO, stable power of 1.91 kW is generated and the residual Gibbs free energy is 1.07 kW. Hence, the corresponding efficiency of ESS drops to 15.59% in Table 4. Furthermore, accompanying with the decrease of dish solar SE efficiency from 43.18% to 25.56% in upstream, the overall efficiency drops to 5.07% under non-ideal condition. The efficiency drop in dish solar module is more significant as compared with RO and PRO modules, for the imperfect regeneration and pressure drop in the heat engine not only increases more heat consumption but also reduces the power output. Thus, improving the performance of dish solar engine by optimizing the heat exchange ability and flow friction will be beneficial for improving the overall energy conversion efficiency.

4. Conclusion

A hybrid energy utilization system, integrating dish solar SE and salinity gradient based energy storage system, was proposed to realize clean and stable power generation from solar energy. Factors impacting the overall system performance are systematically

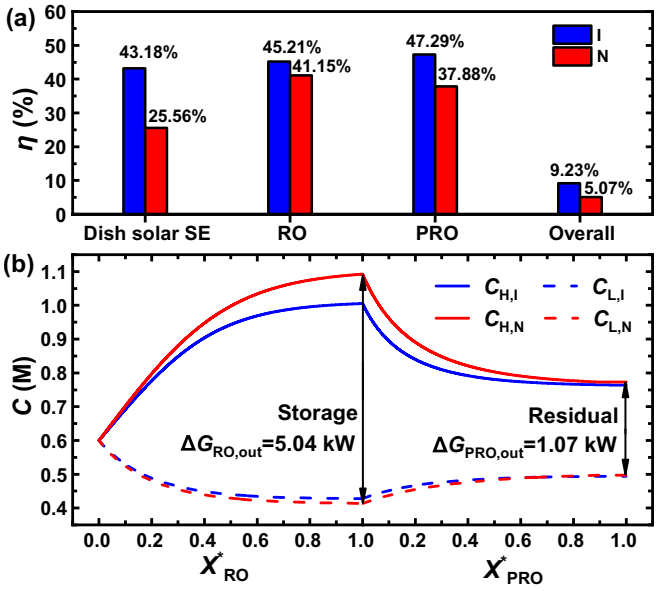

Fig. 12. Efficiency comparison of sub and overall systems in (a) and concentration distribution along the flow direction in RO and PRO under optimal conditions in (b).

investigated. Higher initial concentration of salt water achieves better efficiency of ESS, for it has stronger osmotic pressure difference along the flow direction in PRO. Moreover, optimal ΔP_{RO} and ΔP_{PRO} exist to achieve the maximal energy conversion efficiency under a specified power input from dish solar SE. The optimal ΔP_{RO} represents a state point at which operating pressure and flow rate are both relatively high to achieve strong initial transmembrane water flux and low decreasing slope of draw solution concentration in PRO simultaneously. Meanwhile, the optimal ΔP_{PRO} represents the trade-off of strong specific power ability and high flow rate of extracted water. With numerical optimization work, the maximal ESS efficiency and overall efficiency of 21.38% and 9.23% were achieved under ideal condition. Further considering the detrimental factors, the improvement of optical efficiency increases the receiver temperature to enhance the gas expansion and thermal efficiency of SE. The imperfect heat regeneration and friction loss deteriorates the efficiency of dish solar SE for more heat is required and less shaft power is generated. Thus, power output and efficiency drop from 20.70 kW and 43.18% to 12.25 kW and 25.56% under non-ideal condition. The CP phenomenon in RO and PRO reduces the efficiency of EES for the resistance of transmembrane water flux is increased. As to the solution with initial concentration of 0.6 M, the maximal ESS efficiency and corresponding overall efficiency decrease to 15.59% and 5.07%. For improving the overall energy conversion efficiency in realistic condition, the improvement of dish solar SE performance should be emphasized as compared with RO and PRO. Furthermore, the analysis of concentration distribution indicates the residual Gibbs free energy in PRO is considerable under the optimal condition. Hence, configuration of multistage PRO or additionally applied RED device can be further investigated to enhance the stable power output.

Acknowledgements

We acknowledge the support received from the National Natural Science Foundation of China (51736004,51706076).

Appendix

A1. Adiabatic model of SE

With the divided control volumes of SE as depicted in Fig. 2, the thermodynamic processes are considered operating isothermally in heater and cooler, adiabatically in compression and expansion spaces. Referred from the significant work conducted by Urieli and Berchowitz [32], the basic governing equations of adiabatic model are listed below.

Table A1
Governing equations of adiabatic model

Step	Governing Equation	Number
Volume variation	$V_c = V_{clc} + \frac{1}{2}V_{swc}(1+\cos\theta)$	(A-1)
	$V_e = V_{cle} + \frac{1}{2}V_{swe}(1+\cos(\theta+\alpha))$	(A-2)
Gas pressure	$p = \frac{mR_g}{\left(\frac{V_c}{T_c}+\frac{V_k}{T_k}+\frac{V_r}{T_r}+\frac{V_h}{T_h}+\frac{V_e}{T_e}\right)}$	(A-3)
ODE of operational parameters with respect to crank angle	$\frac{dp}{d\theta} = \frac{-\gamma p\left(\frac{1}{T_{ck}}\frac{dV_c}{d\theta}+\frac{1}{T_{he}}\frac{dV_e}{d\theta}\right)}{\left[\frac{V_c}{T_{ck}}+\gamma\left(\frac{V_k}{T_k}+\frac{V_r}{T_r}+\frac{V_h}{T_h}\right)+\frac{V_e}{T_{he}}\right]}$	(A-4)
	$\frac{dm_c}{d\theta} = \frac{p\frac{dV_c}{d\theta}+\frac{1}{\gamma}V_c\frac{dp}{d\theta}}{RT_{ck}}$	(A-5)
	$\frac{dm_e}{d\theta} = \frac{p\frac{dV_e}{d\theta}+\frac{1}{\gamma}V_e\frac{dp}{d\theta}}{RT_{he}}$	(A-6)
	$\frac{dm_i}{d\theta} = \frac{m_i}{p}\frac{dp}{d\theta}(i=k,r,h)$	(A-7)
	$\frac{dT_i}{d\theta} = T_i\left(\frac{1}{p}\frac{dp}{d\theta}+\frac{1}{V_i}\frac{dV_i}{d\theta}-\frac{1}{m_i}\frac{dm_i}{d\theta}\right)(i=c,e)$	(A-8)
Heat exchanged and work generated per second	$\dot{Q}_h = F\int_0^{2\pi}\left[\frac{V_h c_v}{R_g}\frac{dp}{d\theta}-c_p\left(T_h\frac{m_{rh}'}{d\theta}-T_{he}\frac{m_{he}'}{d\theta}\right)\right]d\theta$	(A-9)
	$\dot{Q}_r = F\int_0^{2\pi}\left[\frac{V_r c_v}{R_g}\frac{dp}{d\theta}-c_p\left(T_k\frac{m_{kr}'}{d\theta}-T_h\frac{m_{rh}'}{d\theta}\right)\right]d\theta$	(A-10)
	$\dot{Q}_k = F\int_0^{2\pi}\left[\frac{V_k c_v}{R_g}\frac{dp}{d\theta}-c_p\left(T_{ck}\frac{m_{ck}'}{d\theta}-T_k\frac{m_{kr}'}{d\theta}\right)\right]d\theta$	(A-11)
	$P = F\left[\int_0^{2\pi}\left(p\frac{dV_c}{d\theta}\right)d\theta+\int_0^{2\pi}\left(p\frac{dV_e}{d\theta}\right)d\theta\right]$	(A-12)

According to Ref. [32], the main calculation procedure of adiabatic model is to solve the correct gas temperature in expansion and compression spaces. For the thermodynamic cycle is a closed loop, the initial temperature in expansion and compression space equals to the final temperature in expansion and compression space respectively as the shaft rotates by a round. With the correct temperature being solved, the heat transferred at hot and cold ends, power generated can be obtained sequentially.

A2. Model validation

In a realistic dish solar SE, the imperfect regeneration and flow friction loss exist and deteriorate the power output and energy efficiency. Considering the regenerator has an effectiveness of ε_R for heat exchange, the heat absorbed and released can be obtained as Eq. (A-13) and (A-14) to achieve the energy balance in Eqs. (1) and (2).

$$\dot{Q}_h^{'} = \dot{Q}_h + (1-\varepsilon_R)\dot{Q}_r \tag{A-13}$$

$$\dot{Q}_k^{'} = \dot{Q}_k - (1-\varepsilon_R)\dot{Q}_r \tag{A-14}$$

Meanwhile, the pressure drop originated from flow friction in the heat exchangers induces the loss of power output as well. Thus, the realistic power output should be modified as Eq. (A-15).

$$P^{'} = P - F\sum\left(\oint \Delta p_i dV_e\right) \quad (i = h, r, k) \tag{A-15}$$

The simulation result is validated with previously reported experiment [33]. The comparison is listed in Table A2.

Table A2
Model validation for dish solar SE

	T_H(K)	$\dot{Q}_{receiver,loss}$(kW)	$\dot{Q}_h^{'}$(kW)	$P^{'}$(kW)	η_{DS-SE}(%)
Simulation	1134.77	5.27	32.43	12.90	26.92
Experiment [33]	1123.15	6.12	31.63	12.25	25.51
Error	1.03%	−13.89%	2.53%	5.31%	5.53%

In Table A2, the temperature of receiver, heat loss in receiver, heat absorbed by SE, shaft power output and energy efficiency are validated. Results indicate the relative error of heat loss in receiver is −13.89% for the reflection and conduction losses in receiver are neglected for simplicity, the other errors are acceptable to state a reliable simulation result for dish solar SE. As to the concentration polarization, the membrane concentration in RO is modified according to Eq. (A-16).

$$C_{H,RO,m} = C_{H,RO,b}\exp\left(\frac{J_{w,RO}}{k_{RO}}\right) \tag{A-16}$$

Table A3
Model validation for RO

ΔP_{RO}(Pa)	518133	677547	853959	1050130	1322090
Simulation (%)	35.81	48.36	61.58	74.92	88.83
Experiment (%)[34]	38.08	51.13	64.55	77.45	90.22
Error	−5.96%	−5.42%	−4.60%	−3.27%	−1.54%

The RO model was validated with previously reported experimental results. The relative error of recovery rate with the inlet velocity of 0.075 m/s under different operating pressure indicate this model is reliable to simulate the performance of RO module. In the modified model of PRO module, the membrane concentration of draw and feed solutions have Eq. (A-17) and (A-18) which are stated as follows.

$$C_{H,PRO,m} = C_{H,PRO,b}\exp\left(-\frac{J_{w,PRO}}{k_{PRO}}\right) - \frac{B}{J_{w,PRO}}\left(C_{H,PRO,m} - C_{L,PRO,m}\right) \times \left[1-\exp\left(\frac{J_{w,PRO}}{k_{PRO}}\right)\right] \tag{A-17}$$

$$C_{L,PRO,m} = C_{L,PRO,b}\exp\left(KJ_{w,PRO}\right) + \frac{B}{J_{w,PRO}}\left(C_{H,PRO,m} - C_{L,PRO,m}\right) \times \left[\exp\left(KJ_{w,PRO}\right) - 1\right] \tag{A-18}$$

Table A4
Model validation for PRO

C_H(g/L)	35			60		
ΔP_{PRO}(Pa)	318303	656808	979827	324813	664241	982716
Simulation (m/s)	2.95e-6	2.57e-6	2.20e-6	4.59e-6	4.32e-6	4.06e-6
Experiment (m/s)[35]	2.91e-6	2.61e-6	2.32e-6	4.68e-6	4.24e-6	4.31e-6
Error (%)	1.47%	−1.47%	−5.22%	−1.87%	1.85%	−5.91%

The PRO model was validated with the relative experiment, water flux calculated was compared with the experimental results under different operating pressure and concentration of draw solution. The relative error indicates the modified model of PRO is reliable.

Nomenclature

A	Area in dish solar SE m^2, Water permeation coefficient in RO and PRO m /(s •Pa)
$\boldsymbol{B}$	Salt permeability coefficient m /s
c_p	Specific heat at constant pressure J /(kg •K)
$\boldsymbol{C}$	Sunshine concentration ratio in dish solar SE, Salt concentration in RO and PRO mol /m^3
$\boldsymbol{F}$	Rotation frequency of engine shaft Hz
h_c	Convective heat transfer coefficient W /(m^2 •K)
$\boldsymbol{I}$	Solar flux intensity W /m^2
$\boldsymbol{J_w}$	Transmembrane water flux m /s
$\boldsymbol{K}$	Heat transfer ability in dish solar SE W /K , Solute resistivity in PRO s /m
$\boldsymbol{L}$	Length of semipermeable membrane m
$\boldsymbol{m}$	Mass of charged gas in SE kg
$\dot{m}_w$	Mass flow rate of coolant kg /s
$\boldsymbol{N}$	Unit number of RO and PRO
$\boldsymbol{p}$	Pressure of charged gas in SE Pa
$\boldsymbol{P}$	Power output W
$\dot{Q}$	Heat transfer rate W
$\boldsymbol{R}$	Molar gas constant J /(mol •K)
$\boldsymbol{R_g}$	Gas constant J /(kg •K)
$\boldsymbol{S}$	State point
$\boldsymbol{T}$	Temperature K

Tan	Water tank
V	Volume cc
$\dot{V}$	Volume flow rate m^3/s
V_{wind}	Wind velocity m/s
W	Width of semipermeable membrane m
ΔP	Operating pressure difference MPa
$\Delta\pi$	Osmotic pressure difference MPa
ΔG	Gibbs free energy W

Greek Symbols

α	Phase angle rad
γ	Specific heat ratio
ε	Emissivity of solar receiver
ε_R	Effectiveness of regenerator
η	Efficiency %
σ	Stefan Boltzmann constant $W/(m^2 \cdot K^4)$
θ	Crank angle rad

Subscripts

0	Environment
1–18	State turning points
b	Bulk flow
c	Compression space
ck	Interface between compression space and cooler
cl	Clearance volume
Dish	Solar dish
DS-SE	Dish solar SE
e	Expansion space
ERD	Energy recovery device
h	Heat absorbing of gas/Heater
he	Interface between heater and expansion space
H	Hot end in dish solar SE, High salt solution concentration in RO and PRO
I	Ideal condition
in	Inlet
k	Cooler
kr	Interface between cooler and regenerator
l	Heat releasing of gas/Cooler
L	Cold end in dish solar SE, Low salt solution concentration in RO and PRO
M	Mixture
N	Non-ideal condition
out	Outlet
r	Regenerator
rh	Interface between regenerator and heater
R	Receiver
sw	Swept volume
w	Water

Abbreviations

CAES	Compressed air energy storage
CP	Concentration polarization
ESS	Energy storage system
GA	Genetic algorithm
GPS	Generalized pattern search
LINMAP	Linear programming techniques for multidimensional analysis of preference
ODE	Ordinary differential equation
PHS	Pumped hydro storage
PRO	Pressure retarded osmosis
PSO	Particle swarm optimization
PX	Pressure exchanger
RED	Reverse electrodialysis
RO	Reverse osmosis
SE	Stirling engine
SEC	Specific energy consumption $kW \cdot h/m^3$
SWRO	Sea water reverse osmosis

References

[1] Bilgen S. Structure and environmental impact of global energy consumption. Renew Sustain Energy Rev 2014;38:890–902.
[2] Jiang L, Agrawal AK, Taylor RP. Clean combustion of different liquid fuels using a novel injector. Exp Therm Fluid Sci 2014;57:275–84.
[3] Long R, Lai X, Liu Z, Liu W. Direct contact membrane distillation system for waste heat recovery: modelling and multi-objective optimization. Energy 2018;148:1060–8.
[4] Fernández-González D, Ruiz-Bustinza I, González-Gasca C, Piñuela Noval J, Mochón-Castaños J, Sancho-Gorostiaga J, et al. Concentrated solar energy applications in materials science and metallurgy. Sol Energy 2018;170:520–40.
[5] Lai X, Long R, Liu Z, Liu W. A hybrid system using direct contact membrane distillation for water production to harvest waste heat from the proton exchange membrane fuel cell. Energy 2018;147:578–86.
[6] Roumpedakis TC, Christou T, Monokrousou E, Braimakis K, Karellas S. Integrated ORC-Adsorption cycle: a first and second law analysis of potential configurations. Energy 2019;179:46–58.
[7] Liu W, Liu P, Dong ZM, Yang K, Liu ZC. A study on the multi-field synergy principle of convective heat and mass transfer enhancement. Int J Heat Mass Transf 2019;134:722–34.
[8] Liu W, Liu P, Wang JB, Zheng NB, Liu ZC. Exergy destruction minimization: a principle to convective heat transfer enhancement. Int J Heat Mass Transf 2018;122:11–21.
[9] Wang G, Yao Y, Chen Z, Hu P. Thermodynamic and optical analyses of a hybrid solar CPV/T system with high solar concentrating uniformity based on spectral beam splitting technology. Energy 2019;166:256–66.
[10] Aksoy F, Karabulut H. Performance testing of a Fresnel/Stirling micro solar energy conversion system. Energy Convers Manag 2013;75:629–34.
[11] Li Y, Liu G, Liu X, Liao S. Thermodynamic multi-objective optimization of a solar-dish Brayton system based on maximum power output, thermal efficiency and ecological performance. Renew Energy 2016;95:465–73.
[12] Ahmadi MH, Mohammadi AH, Dehghani S, Barranco-Jiménez MA. Multi-objective thermodynamic-based optimization of output power of Solar Dish-Stirling engine by implementing an evolutionary algorithm. Energy Convers Manag 2013;75:438–45.
[13] Cheng C-H, Yang H-S. Optimization of rhombic drive mechanism used in beta-type Stirling engine based on dimensionless analysis. Energy 2014;64:970–8.
[14] Ipci D, Karabulut H. Thermodynamic and dynamic analysis of an alpha type Stirling engine and numerical treatment. Energy Convers Manag 2018;169:34–44.
[15] Ahmadi MH, Sayyaadi H, Dehghani S, Hosseinzade H. Designing a solar powered Stirling heat engine based on multiple criteria: maximized thermal efficiency and power. Energy Convers Manag 2013;75:282–91.
[16] Ahmadi MH, Ahmadi MA, Mellit A, Pourfayaz F, Feidt M. Thermodynamic analysis and multi objective optimization of performance of solar dish Stirling engine by the centrality of entransy and entropy generation. Int J Electr Power Energy Syst 2016;78:88–95.
[17] Aksoy F, Karabulut H, Çınar C, Solmaz H, Özgören YÖ, Uyumaz A. Thermal performance of a Stirling engine powered by a solar simulator. Appl Therm Eng 2015;86:161–7.
[18] Carrillo Caballero GE, Mendoza LS, Martinez AM, Silva EE, Melian VR, Venturini OJ, et al. Optimization of a Dish Stirling system working with DIR-type receiver using multi-objective techniques. Appl Energy 2017;204:271–86.
[19] Ferreira AC, Nunes ML, Teixeira JCF, Martins LASB, Teixeira SFCF. Thermodynamic and economic optimization of a solar-powered Stirling engine for micro-cogeneration purposes. Energy 2016;111:1–17.
[20] Kadri Y, Hadj Abdallah H. Performance evaluation of a stand-alone solar dish Stirling system for power generation suitable for off-grid rural electrification. Energy Convers Manag 2016;129:140–56.
[21] He W, Wang J. Feasibility study of energy storage by concentrating/desalinating water: concentrated Water Energy Storage. Appl Energy 2017;185:872–84.
[22] Long R, Lai X, Liu Z, Liu W. A continuous concentration gradient flow electrical energy storage system based on reverse osmosis and pressure retarded osmosis. Energy 2018;152:896–905.
[23] Lai X, Long R, Liu Z, Liu W. Stirling engine powered reverse osmosis for brackish water desalination to utilize moderate temperature heat. Energy 2018;165:916–30.
[24] Guo C, Chang H, Liu B, He Q, Xiong B, Kumar M, et al. A combined ultrafiltration–reverse osmosis process for external reuse of Weiyuan shale gas flowback and produced water. Environ Sci: Water Res. Technol. 2018;4(7):942–55.
[25] He W, Wang Y, Shaheed MH. Modelling of osmotic energy from natural salt gradients due to pressure retarded osmosis: effects of detrimental factors and flow schemes. J Membr Sci 2014;471:247–57.
[26] Banchik LD, Sharqawy MH, Lienhard JH. Effectiveness-mass transfer units

(ε-MTU) model of a reverse osmosis membrane mass exchanger. J Membr Sci 2014;458:189–98.
[27] He W, Wang Y, Shaheed MH. Maximum power point tracking (MPPT) of a scale-up pressure retarded osmosis (PRO) osmotic power plant. Appl Energy 2015;158:584–96.
[28] Yip NY, Elimelech M. Thermodynamic and energy efficiency analysis of power generation from natural salinity gradients by pressure retarded osmosis. Environ Sci Technol 2012;46(9):5230–9.
[29] Prante JL, Ruskowitz JA, Childress AE, Achilli A. RO-PRO desalination: an integrated low-energy approach to seawater desalination. Appl Energy 2014;120:104–14.
[30] Wan CF, Chung T-S. Energy recovery by pressure retarded osmosis (PRO) in SWRO–PRO integrated processes. Appl Energy 2016;162:687–98.
[31] Banan Sadeghian R, Pantchenko O, Tate D, Shakouri A. Miniaturized concentration cells for small-scale energy harvesting based on reverse electrodialysis. Appl Phys Lett 2011;99(17):173702.
[32] Urieli I, Berchowitz DM. Stirling cycle engine analysis: A. Hilger Bristol. 1984.
[33] Reinalter W, Ulmer S, Heller P, Rauch T, Gineste J-M, Ferriere A, et al. Detailed performance analysis of a 10kW Dish stirling system. J Sol Energy Eng 2008;130(1):011013.
[34] Song L, Tay K. Performance prediction of a long crossflow reverse osmosis membrane channel. J Membr Sci 2006;281(1–2):163–9.
[35] Achilli A, Cath TY, Childress AE. Power generation with pressure retarded osmosis: an experimental and theoretical investigation. J Membr Sci 2009;343(1–2):42–52.